

An optimized and highly repeatable MRI acquisition and processing pipeline for quantitative susceptibility mapping in the head-and-neck region

Anita Karsa^{1,2}   | Shonit Punwani² | Karin Shmueli^{1,2} 

¹Department of Medical Physics and Biomedical Engineering, University College London, London, United Kingdom

²Centre for Medical Imaging, University College London, London, United Kingdom

Correspondence

Anita Karsa, Department of Medical Physics and Biomedical Engineering, University College London, Gower Street, London, WC1E 6BT, United Kingdom.
Email: anita.karsa.14@ucl.ac.uk

Present address

Anita Karsa and Karin Shmueli, Department of Medical Physics and Biomedical Engineering, University College London, Gower Street, London, WC1E 6BT, United Kingdom

Funding information

UCL Centre for Doctoral Training in Medical Imaging, Grant/Award Number: EP/L016478/1; ERC Consolidator Grant DiSCo MRI SFN, Grant/Award Number: 770939

Purpose: Quantitative Susceptibility Mapping (QSM) is an emerging technique sensitive to disease-related changes including oxygenation. It is extensively used in brain studies and has increasing clinical applications outside the brain. Here we present the first MRI acquisition protocol and QSM pipeline optimized for the head-and-neck region together with a repeatability analysis performed in healthy volunteers.

Methods: We investigated both the intrasession and the intersession repeatability of the optimized method in 10 subjects. We also implemented two, Tikhonov-regularisation-based susceptibility calculation techniques that were found to have higher contrast-to-noise than existing methods in the head-and-neck region. Repeatability was evaluated by calculating the distributions of susceptibility differences between repeated scans and the corresponding minimum detectable effect sizes (MDEs).

Results: Deep brain regions had higher QSM repeatability than neck regions. As expected, intrasession repeatability was generally better than intersession repeatability. Susceptibility maps calculated using projection onto dipole fields for background field removal were more repeatable than using the Laplacian boundary value method in the head-and-neck region. Small (short-axis diameter <5 mm) lymph nodes had the lowest repeatability (MDE = 0.27 ppm) as imperfect segmentation included some of the surrounding paramagnetic fatty fascia, highlighting the importance of accurate region delineation. MDEs in the larger lymph nodes (0.16 ppm), submandibular glands (0.10 ppm), and especially the parotid glands (0.06 ppm) were much lower, comparable to those of the brain regions.

Conclusions: The high repeatability of the acquisition and pipeline optimized for QSM will facilitate clinical studies in the head-and-neck region.

KEYWORDS

head and neck, lymph node, parotid gland, QSM, repeatability, submandibular gland, susceptibility mapping

This is an open access article under the terms of the Creative Commons Attribution License, which permits use, distribution and reproduction in any medium, provided the original work is properly cited.

© 2020 The Authors. *Magnetic Resonance in Medicine* published by Wiley Periodicals LLC on behalf of International Society for Magnetic Resonance in Medicine

1 | INTRODUCTION

Quantitative Susceptibility Mapping (QSM) is a recent technique that calculates tissue magnetic susceptibility maps from MRI phase images.¹⁻⁴ Susceptibility maps can reveal disease-related changes in tissue iron, myelin and calcium content, and venous oxygenation.⁵⁻⁹ Therefore, QSM shows promise for several clinical applications¹⁰ including in Multiple Sclerosis,¹¹⁻¹³ Parkinson's¹⁴⁻¹⁶ and Huntington's¹⁷ diseases.

Recently, this technique has been increasingly applied in parts of the body other than the brain, for example, to detect calcifications, or measure liver iron content^{7,18-20} As QSM is a complicated, multi-step processing pipeline with a plethora of state-of-the-art methods for each step,²¹⁻²³ the pipeline needs to be carefully optimized for each anatomical region. Furthermore, it has been shown that MRI acquisition parameters, such as image resolution or coverage,²⁴⁻²⁶ also influence the quality of the resulting susceptibility maps. Therefore, the acquisition protocol also needs to be tailored for different anatomical regions. Finally, though many studies have shown QSM to be highly repeatable in the brain,²⁷⁻³² repeatability analyses of QSM in anatomical regions outside the brain have not yet been performed.

Here we present the first MRI acquisition protocol and susceptibility mapping pipeline optimized for the head-and-neck (HN) region.³³ Performing QSM in this anatomical region is particularly challenging due to unavoidable motion artifacts (eg, due to swallowing), large background fields induced by the many tissue-air interfaces (eg, oropharyngeal air spaces), and chemical-shift artifacts introduced by fatty tissue. We also present two implementations (one based on direct k-space inversion and one based on iterative fitting in image space) of the Tikhonov-regularized susceptibility calculation method^{3,34} including correction for inherent susceptibility underestimation³⁵ that outperformed other state-of-the-art susceptibility calculation methods in the HN region in terms of contrast and noise. We evaluated the repeatability of this optimized acquisition and QSM pipeline in healthy volunteers.³⁶ We investigated both the intrasession and intersession repeatability of the susceptibility in brain and neck regions and compared the mean and median susceptibility as summary measures in regions of interest (ROIs).

2 | METHODS

2.1 | Data acquisition

The local ethics committee approved this study and informed consent was obtained from all participants.

Multi-echo head-and-neck (HN) images were acquired in 10 healthy volunteers (age range: 23-30 years, seven females and three males) at 3-T (Achieva, Philips Healthcare, NL)

using a 3D gradient-echo pulse sequence tailored for structural HN QSM and a 16-channel HN receiver coil.³³ Coronal orientation (readout = head-foot direction) with a field-of-view = 24 cm × 24 cm × 22 cm was used to avoid wrap-around artifacts. A SENSE acceleration factor = 2³⁷ in the right-left (first phase encoding) direction and 1.25 mm isotropic resolution were selected based on a preliminary comparison of images (Supporting Information Figures S1 and S2) acquired at different resolutions (1-1.5 mm isotropic voxels²⁶⁷) and SENSE acceleration factors (1-2 in both phase encoding directions). These optimized parameters provided sufficient signal-to-noise ratio while, at the same time, providing susceptibility maps that were not substantially influenced by partial volume effects²⁶ or motion artifacts. Using in-phase echo timing ($TE_1 = \Delta TE = 4.61$ ms) was found to be the most robust way to remove the chemical shift-induced phase differences between fatty and water-based tissues.²⁰ Four echoes, TR = 22 ms, and flip angle = 12° were selected for a clinically feasible scan time of 6 minutes and 4 seconds. Vendor-supplied first order gradient-moment nulling on the first echo (flow compensation) was used which resulted in first order gradient moments at all four echo times being very close to zero.

All 10 volunteers were scanned using the parameters described above at two sessions a week apart, three times per session to investigate both intersession and intrasession repeatability of susceptibility mapping in the HN region in healthy volunteers (Figure 3B).

2.2 | Susceptibility mapping pipelines

Susceptibility maps were calculated from all complex, multi-echo images using susceptibility mapping pipelines optimized for HN images.³³ Nonlinear field fitting^{38,39} was used to estimate the field map as this technique can be applied directly to the complex data without having to unwrap the acquired phase images at each echo separately. Although almost instantaneous, Laplacian-based techniques do not preserve the linearity of the phase over echo times⁴⁰ so, for accurate results, they can only be applied after field fitting. Separate unwrapping would require the use of a region growing approach that could take up to 20 minutes all echoes in a multi-echo HN image.⁴¹ Nonlinear field fitting provided a quick and robust way of estimating field maps. The residual wraps were then removed using LPU as this method proved to be faster and more robust in the highly wrapped HN region than region-growing techniques (Supporting Information Figure S3).

In a preliminary optimisation of background field removal techniques for the HN region, we compared a range of techniques throughout a numerical HN phantom. Our results in the brain were in good agreement with the more

comprehensive comparison of Schweser et al.²² We found that Projection onto Dipole Fields⁴² (PDF) and the Laplacian Boundary Value (LBV) method⁴³ provided the most accurate local field maps. Here we compared these two background field removal techniques in terms of QSM repeatability. HN tissue masks were generated by thresholding the inverse noise map (which is an output of the nonlinear fitting algorithm³⁹ and is calculated using noise propagation³⁴) at the mean of the inverse noise across the image to exclude areas of high noise. This simple method provided suitable tissue masks for robust background field removal in each volunteer.

We selected candidate susceptibility calculation methods based on a previous comparison performed in in vivo HN images (Figure 1). The methods we had compared were Truncated K-space Division¹ (TKD, using a threshold of

$\delta = 2/3$ and correction for susceptibility underestimation³⁵), Morphology Enabled Dipole Inversion⁴⁴ (MEDI, with a regularisation parameter of $\lambda = 160$ determined using L-curve optimisation⁴⁵), and iLSQR⁴⁶ as these are high-performing and widely used techniques within the QSM community.²³ We also included Tikhonov regularisation^{3,23,34} as a candidate susceptibility calculation technique. This method aims to solve the following minimisation problem:

$$\arg \min_{\chi} \|MW(B_{local} - B_0 \cdot (d * \chi))\|_2^2 + \alpha \|\chi\|_2^2 \quad (1)$$

where χ is the susceptibility map, d is the unit dipole field, B_{local} is the local field map obtained after the background field removal step, B_0 is the main magnetic field strength, M is a binary

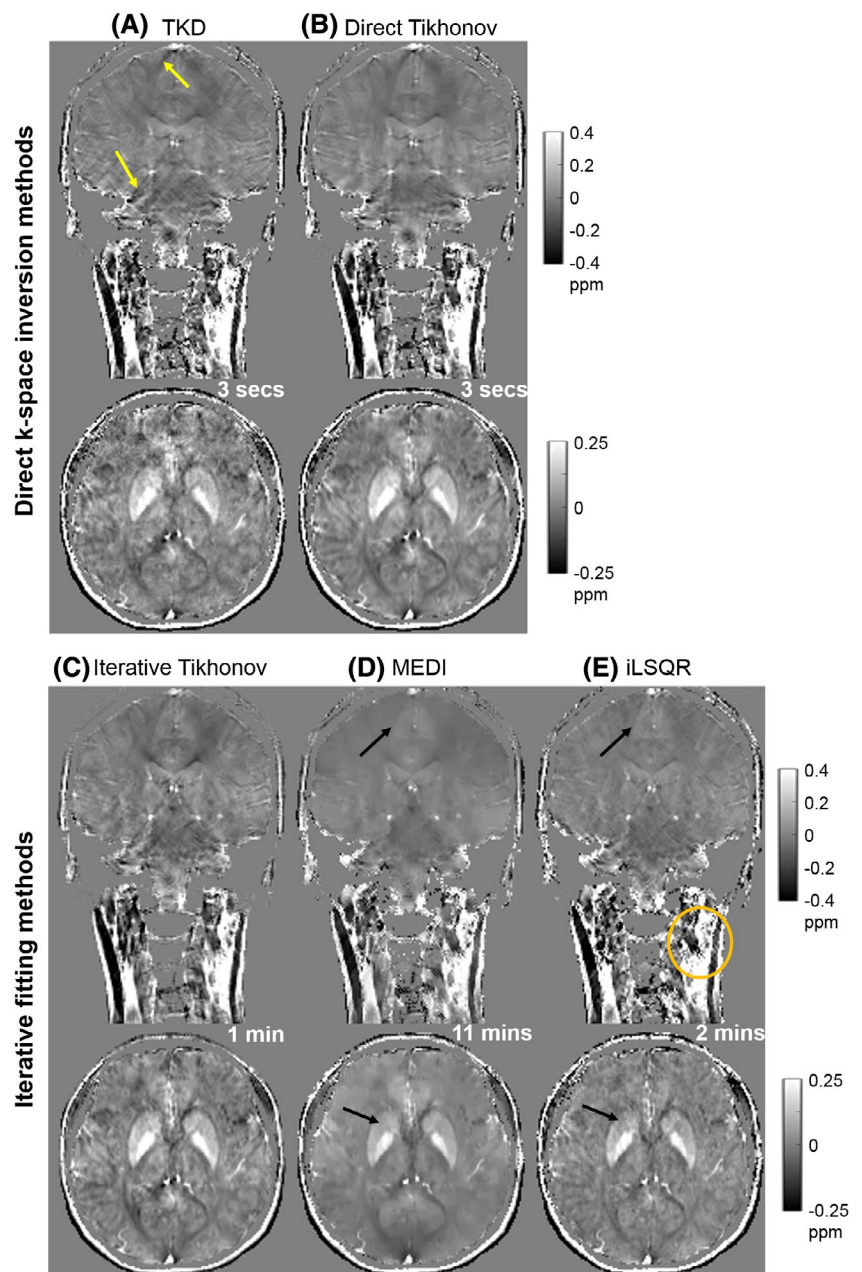


FIGURE 1 Preliminary comparison of TKD (A), direct Tikhonov (B), iterative Tikhonov (C), MEDI (D), and iLSQR (E) as susceptibility calculation methods in the head and neck.³³ The computation times measured on a PC with an Intel Xeon processor with 32 GB RAM and an NVIDIA Quadro K420 GPU are displayed in the bottom right corner of each image. The yellow arrows shows streaking artifacts in the TKD result. The black arrows indicate lower susceptibility contrast of the putamen and in the white matter in the MEDI and iLSQR results. The orange ellipses highlight noisy regions in the neck in the iLSQR result

tissue mask, W is a weighting term accounting for the spatially varying noise level, and α is the regularisation parameter. This problem can be solved either iteratively using conjugate gradient minimisation,^{34,47} or, if both the binary tissue mask (M) and the weighting matrix (W) are set to 1, χ can be calculated directly in k-space^{3,23} using:

$$\chi = \mathcal{F}^{-1} \left\{ \frac{1}{B_0} \cdot \frac{D}{D^2 + \alpha} \cdot \mathcal{F} \{ B_{local} \} \right\} \quad (2)$$

where \mathcal{F} and \mathcal{F}^{-1} denote the Fourier and inverse Fourier transform, respectively, and $D = \mathcal{F} \{ d \}$ is the dipole field in k-space. Here we included correction for susceptibility underestimation as described in³⁵ by multiplying the results of both approaches by $1/p(\mathbf{0}, \alpha)$ where the point-spread function is:

$$p(\mathbf{r}, \alpha) = \mathcal{F}^{-1} \left\{ \frac{D^2}{D^2 + \alpha} \right\} \quad (3)$$

Both techniques were included in the preliminary comparison (Figure 1) with $\alpha = 0.11$ and 0.04 (determined using L-curve optimisation⁴⁵) for the iterative and direct approaches, respectively, and $W =$ the inverse noise map^{34,39} for the iterative version. For the iterative version, the conjugate gradient minimisation was stopped when the norm of the residuals decreased below 6% of the norm of the local field map. Generally, the fitted susceptibility map did not change much for iterations close to this point and much later stopping led to overfitting. The same tissue mask was used as for background field removal as described above. Zero padding to a matrix size of 256×256 (from the original $192 \times 192 \times 176$) was applied before using either TKD or the direct Tikhonov susceptibility

calculation technique to avoid errors introduced by the Fourier and inverse Fourier transforms. Though TKD is a fast technique, it provided susceptibility maps with a substantial amount of streaking (Figure 1A, yellow arrows). The results of both MEDI and iLSQR had much lower susceptibility contrast compared to the other methods (Figure 1D-E, black arrows).^{23,33} Moreover, MEDI took about 11 minutes to process a HN image on a PC with an Intel Xeon processor with 32 GB RAM and an NVIDIA Quadro K420 GPU and the iLSQR result was very noisy in the neck (Figure 1E, orange ellipse). Both Tikhonov-based methods provided HN susceptibility maps with sufficiently reduced streaking artifacts and noise in a reasonable amount of time (<1 minute) for clinical application. Therefore, here we compared these two Tikhonov-based susceptibility calculation techniques in terms of susceptibility repeatability.

2.3 | Regions of interest

We evaluated the repeatability of susceptibility values in ROIs in both the brain, to allow comparison with previous studies, and in the neck that was the focus of this study. Figure 2 shows the pipeline for ROI segmentation. As a first step, ROIs were delineated in the first acquired image (the first image of the first scanning session). Brain regions (thalamus, caudate nucleus, putamen, and globus pallidus) were automatically segmented using FSL FIRST⁴⁸ on the first-echo magnitude images (Figure 2A) since these had the most similar contrast to T_1 -weighted images for which FSL FIRST is optimized (FSL FIRST failed to terminate when applied to any of the other three echoes). This automatic segmentation worked well for most volunteers, but failed in two cases

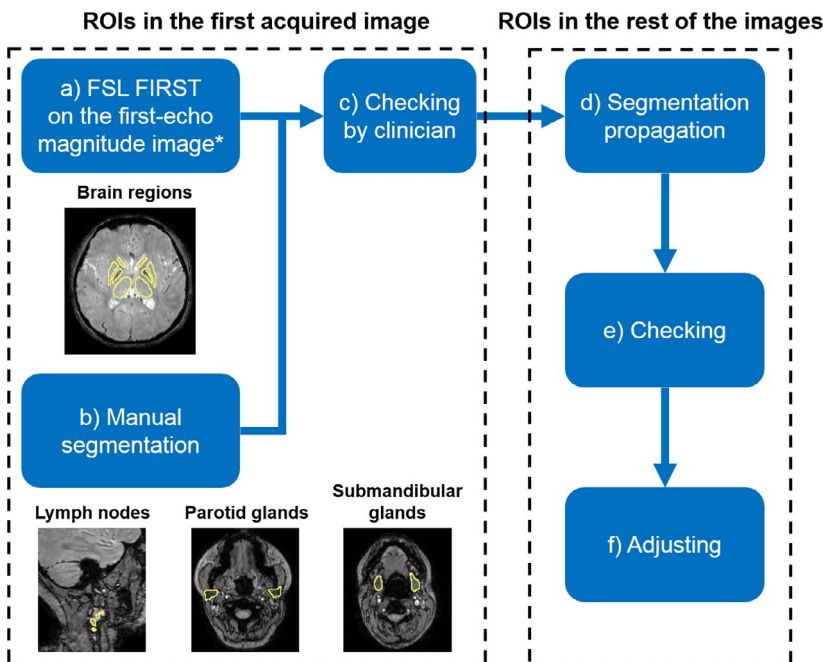


FIGURE 2 Pipeline for segmenting regions of interest in the brain and HN. *Delineation of the brain ROIs was done manually for two volunteers where FSL FIRST did not work. Note that the example ROIs are overlaid on the last-echo magnitude images

because these volunteers had largely different head shapes from the rest of the subjects. In these two cases, the brain ROIs were manually segmented using ITK-SNAP^{49,50} in single, axial slices on the last-echo magnitude images as these had the best contrast.

Three types of healthy lymph nodes were segmented manually (using ITK-SNAP) on the last-echo magnitude image (Figure 2B): small and medium nodes (see next section for the exact definition), and the insides of larger nodular structures leaving a 1-2 voxel margin around the ROIs. The latter are tightly packed lymph nodes below the submandibular glands which have larger overall volumes than regular, individual lymph nodes allowing for the few mm margin in the segmentation. Two of each of these three ROI types were identified and delineated per volunteer wherever possible. The parotid and submandibular glands were also manually segmented in single, axial slices (Figure 2B). All ROIs delineated in the first acquired images were checked (Figure 2C) by an experienced radiologist (S.P.).

ROIs in the remaining five images (the remaining two images from the first session and all three images from the second session) were segmented by propagating the initial segmentation using a MATLAB-based, b-spline image registration tool⁵¹⁻⁵³ (Figure 2D). The last-echo magnitude image of the first image was non-rigidly registered to the last-echo magnitude images from the other acquisitions in the same subject and the resulting transformations were used to warp all ROIs segmented in the first acquired image. The last-echo magnitude images were used as these had the best contrast in the deep gray matter regions and around the glands and lymph nodes. All ROIs were checked visually (Figure 2E) and manually adjusted in ITK-SNAP if necessary (Figure 2F).

Mean and median susceptibility values were calculated in all ROIs to compare the repeatability of these different measures in healthy volunteers. Note that the susceptibility maps were not explicitly referenced to any particular tissue. However, both Tikhonov-based susceptibility calculation techniques produced susceptibility maps with zero integrals. Therefore, all resulting susceptibility maps were implicitly referenced to the average susceptibility across each image volume.

We also manually segmented regions of subcutaneous fat at the back of the neck, the semispinalis capitis muscle, and the masseter muscle in single, axial slices of all 10 healthy subjects to assess the reliability of our susceptibility maps in the neck. These ROIs were drawn in the last-echo magnitude image of the first scan of each volunteer and mean susceptibilities were calculated in each region.

The intrasession and intersession subject movement was measured by calculating the translation (in all three directions: dx , dy , and dz), and the azimuthal (toward the z axis: $d\theta$) and polar (about the z axis: $d\phi$) rotations of the skull from the aforementioned non-rigid transformations used for ROI propagation.

2.4 | Repeatability analysis

Before performing the repeatability analysis, the small and medium nodes were classified based on their actual volumes (VOL): small nodes $< 300 \text{ mm}^3$; medium nodes $> 300 \text{ mm}^3$. This threshold was set based on the distribution of nodal sizes to make sure that there were a similar number of lymph nodes in both categories (about 20 in each category). An alternative classification was also performed based on the short axis diameters (SAD) of the nodes: small nodes $< 5 \text{ mm}$; medium nodes $> 5 \text{ mm}$, as this is the size measure most frequently used in clinical practice. Again, about 20 nodes were assigned to each group. We also segmented a similar number (17) of large nodular structures. Note that while SAD is the more common size measure in clinical practice, VOL is proportional to the number of voxels in the ROI which is expected to be more closely related to the accuracy of the calculated mean or median values.

To evaluate the intrasession repeatability, differences of the measured mean and median susceptibilities were calculated between all pairs of scans acquired in the same session (Figure 3B, orange arrows) and the distributions of these differences were considered for each ROI type. If the intrasession repeatability is high, these distributions are expected to be narrow with a mean close to zero. Similarly, to evaluate intersession repeatability, differences of the measured mean

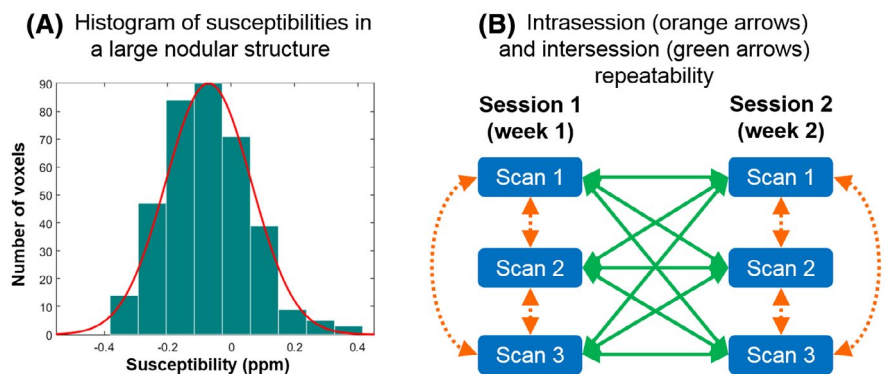


FIGURE 3 Susceptibility histogram with a fitted Gaussian distribution in a typical large nodal structure (A) and diagram of the comparisons performed (B) for the intrasession (orange dotted arrows) and intersession (green arrows) repeatability analysis

and median susceptibilities were computed between all pairs of scans of the same volunteer acquired in different sessions (Figure 3B, green arrows).

To quantify the repeatability in terms of the minimum susceptibility difference it should be possible to detect, the minimum detectable effect (MDE)⁵⁴ was calculated for all ROI types based on the standard deviations (SDs) of the distributions of susceptibility differences, assuming a Gaussian shape, a type I error rate of $\alpha = 0.05$ and a type II error rate of $\beta = 0.2$ using the following equation:

$$\text{MDE} = \underbrace{1.65 \cdot \text{SD}}_{\text{accounting for type I error, } \alpha=0.05} + \underbrace{0.84 \cdot \text{SD}}_{\text{accounting for type II error, } \beta=0.2} \quad (4)$$

A lower SD and, consequently, lower MDE corresponds to a better repeatability.

2.5 | The effect of fatty fascia on the measured susceptibility of lymph nodes

Many of the healthy lymph nodes were located within the fatty fascia between muscle sheets. However, fat has been repeatedly shown to have a much higher susceptibility than other tissues such as muscle.^{7,18,19,55} Therefore, the surrounding fat could confound the susceptibility measurements of

lymph nodes, for example, if voxels of the fatty fascia are included in the ROI by mistake, due to partial volume effects, or if there are susceptibility artifacts originating from the large susceptibility gradient between the lymph node and the fatty fascia. These effects are expected to be more substantial for smaller nodes which have a higher surface-to-volume ratio. To investigate this issue, susceptibility histograms of all voxels pooled according to node size type were compared.

3 | RESULTS

3.1 | Susceptibility maps in the head and neck

Figures 4 and 5 show example axial and cropped coronal slices of the last-echo magnitude image and susceptibility map in the HN region of the same representative volunteer. As expected, deep gray matter nuclei have increased susceptibilities compared to the surrounding tissue due to their elevated iron content (Figure 4B, black arrows) leading to improved contrast when compared to the magnitude image (Figure 4A, black arrows). The yellow arrows in Figure 4 indicate the parotid glands and the masseter muscles which are clearly discernible from the surrounding subcutaneous fat in both the magnitude image and the susceptibility map. Note that parotid lymph nodes are only visible in the

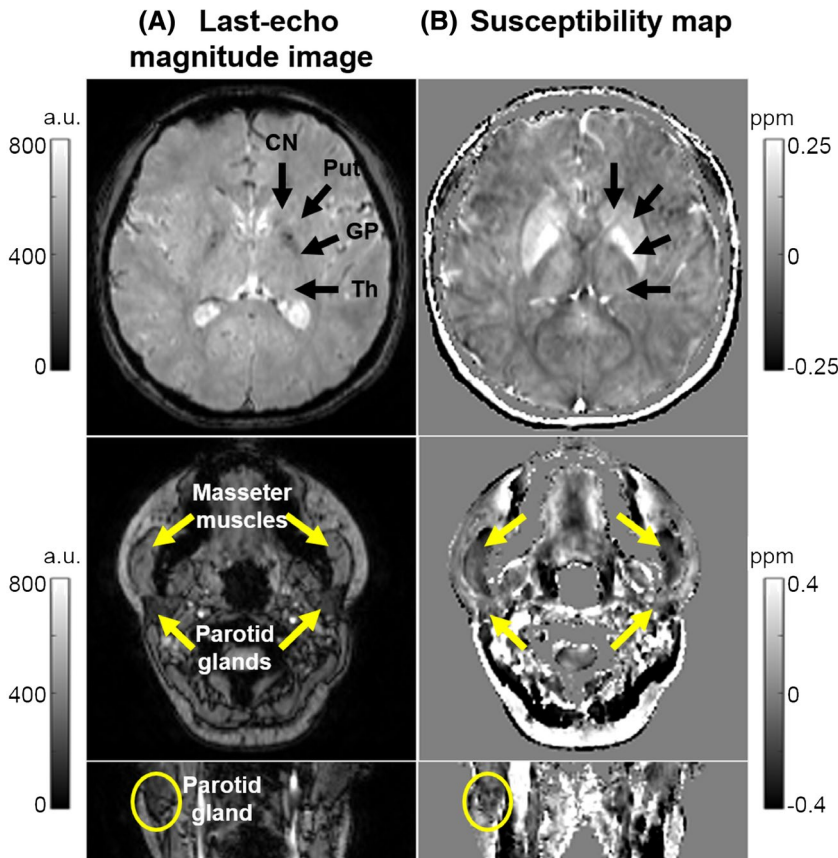
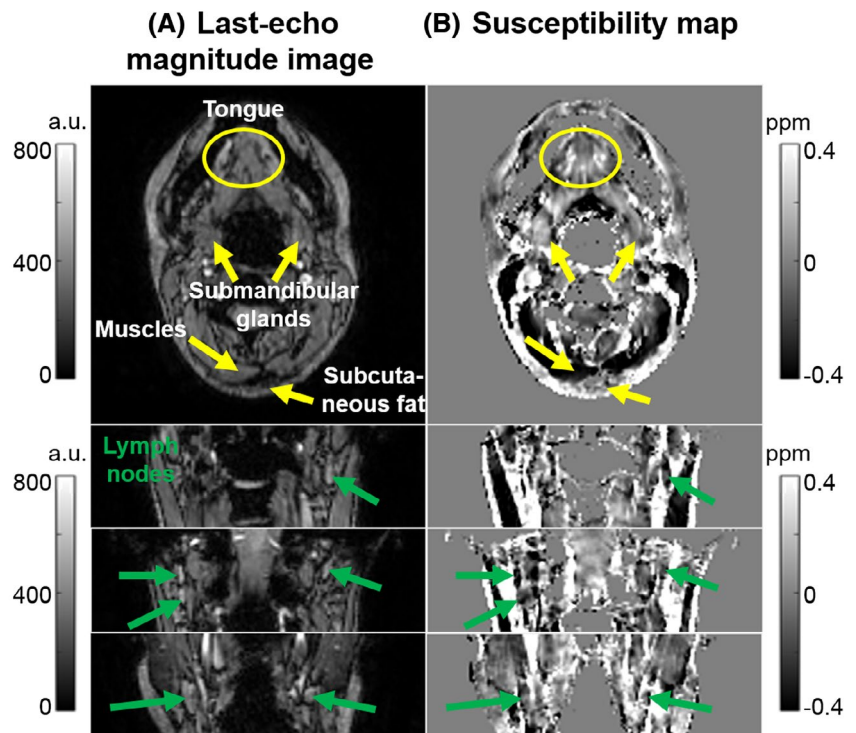


FIGURE 4 Anatomical structures visible in susceptibility maps of the HN. Last-echo magnitude image (A) and susceptibility map (B) calculated using PDF and direct k-space inversion with Tikhonov regularisation in a representative healthy volunteer. The arrows and ellipses indicate various anatomical regions in the brain and the neck. Note that all coronal images are cropped

FIGURE 5 Lymph nodes and other structures visible in susceptibility maps of the HN. Last-echo magnitude image (A) and susceptibility map (B) calculated using PDF and direct k-space inversion with Tikhonov regularisation in a representative healthy volunteer. The arrows and ellipses indicate various anatomical regions and lymph nodes in the neck. Note that all coronal images are cropped



susceptibility map (Figure 4, yellow ellipses). The yellow arrows in Figure 5 indicate the submandibular glands and the high susceptibility contrast between muscles and subcutaneous fat in the neck. The yellow ellipses highlight the heterogeneous susceptibility across the tongue that is consistent with the anatomy seen in the magnitude image. The green arrows in Figure 5 indicate various healthy lymph nodes in the neck. Note that many of these are surrounded by paramagnetic (bright) fatty fascia.

The measured susceptibilities in the subcutaneous fat at the back of the neck, the semispinalis capitis muscle, and the masseter muscle were 0.29 ± 0.14 ppm, -0.25 ± 0.22 ppm, and -0.18 ± 0.07 ppm, respectively. These values correspond to the mean and standard deviation across subjects, respectively.

3.2 | Subject movement

The intrasession movements were very small: dx , dy , and dz were 0.4, 0.4, and 0.5 mm on average and up to 1.7, 1.1, and 2.6 mm, respectively. The intrasession $d\theta$ and $d\phi$ were both 0.3° on average and 1° and 0.8° in the most extreme cases, respectively. The intersession dx , dy , and dz were 2.9, 4.7, and 2.6 mm on average and up to 8.1, 10.8, and 7.6 mm, respectively, while $d\theta$ and $d\phi$ were 2.0° and 1.7° on average and 4.3° and 3.8° in the most extreme cases. Note that even the intersession movement was less than 1 cm in all three directions because the 16-channel Philips HN receiver coil is fairly tight when the subject has the ear defenders on

resulting in reasonably repeatable subject positioning within the coil with no additional effort.

3.3 | Comparison of different QSM processing pipelines and summary measures

Figure 6 top shows the comparison of the PDF and LBV background field removal methods in terms of intrasession susceptibility repeatability in the HN. Here, susceptibility maps were calculated using direct k-space inversion with Tikhonov regularisation. The means of all the susceptibility difference distributions were very close to zero (within ± 0.005 ppm) except in the small nodes and the globus pallidus. Susceptibility repeatability using PDF was higher than with LBV in all ROI types except in the globus pallidus (Figure 6 top, blue ellipse). We observed similar trends when using iterative Tikhonov regularisation to calculate susceptibility maps and for intersession comparisons as well (Supporting Information Figures S4-S6).

A similar comparison between direct k-space inversion and iterative fitting (with PDF for background field removal) is displayed in Figure 6 bottom. Iterative fitting in image space performed slightly better in terms of repeatability in small and medium nodes, and the parotid and submandibular glands. However, direct k-space inversion provided marginally improved results in the larger nodular structures and all brain ROIs. Intersession repeatability using these two susceptibility calculation methods was also

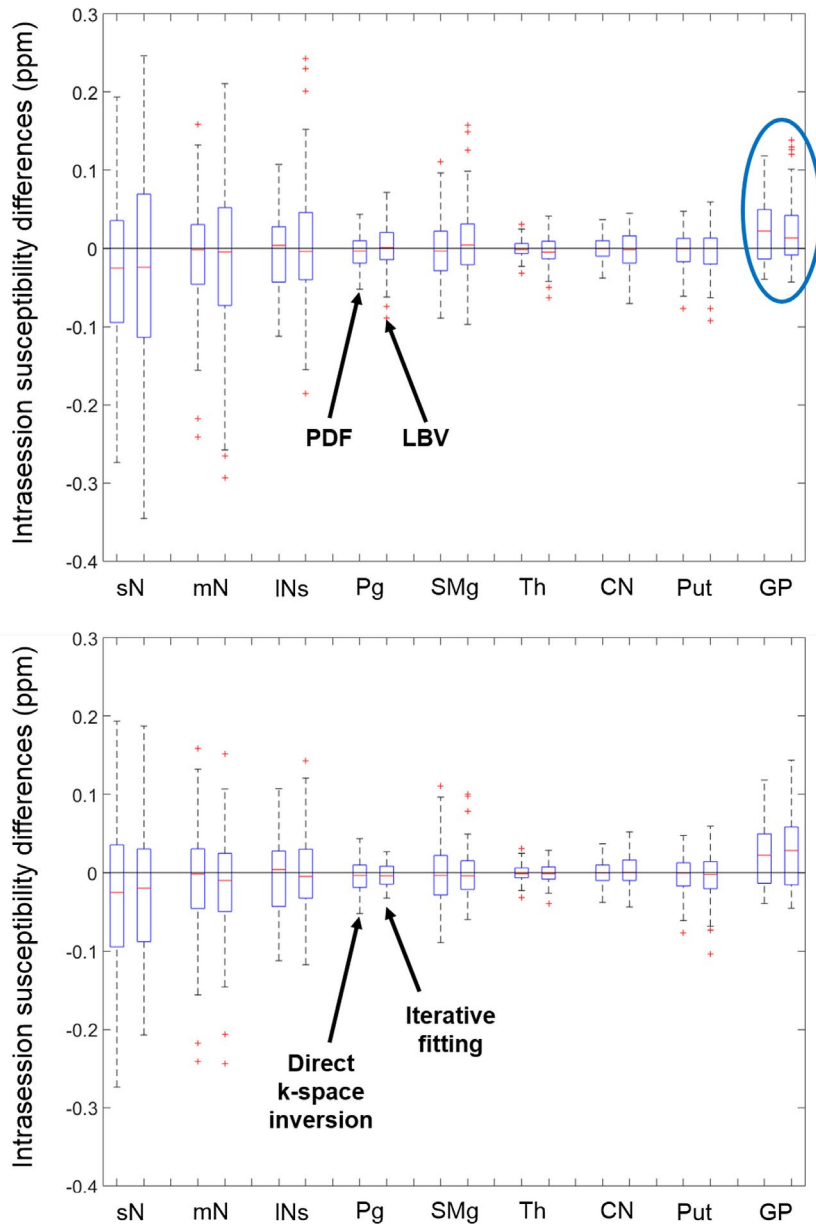


FIGURE 6 A comparison of the intrasession repeatability of the mean susceptibility calculated using different background field removal techniques (top) and Tikhonov-based regularisation susceptibility calculation methods (bottom). Box plots of intrasession mean susceptibility differences in different ROI types (red lines: medians, boxes: 25th and 75th percentiles, whiskers: most extreme data points not considered outliers, red crosses: outliers): sN, small nodes ($VOL < 300 \text{ mm}^3$), mN, medium nodes ($VOL > 300 \text{ mm}^3$), INs, large nodular structures; Pg, parotid glands; SMg, submandibular glands; Th, thalamus; CN, caudate nucleus; Put, putamen; GP. For each ROI type, distributions on the left and right sides correspond to susceptibility maps obtained using PDF or LBV (top) and direct k-space inversion or iterative fitting (bottom), respectively (see arrows). Direct k-space inversion with Tikhonov regularisation and PDF were used for susceptibility calculation and background field removal for the top and bottom graphs, respectively

very similar to Figure 6 bottom (Supporting Information Figure S7).

In all previous comparisons, the mean susceptibility in each ROI was used as the summary measure. Figure 7 shows that there was no substantial difference in intrasession susceptibility repeatability between using the mean or median susceptibility measured in each ROI. Similar results were observed for intersession susceptibility repeatability (not shown).

3.4 | Histograms of healthy lymph nodes of various sizes

Figure 8A shows the distributions of intrasession mean susceptibility differences calculated using PDF and direct

k-space inversion with Tikhonov regularisation. The arrow indicates that higher repeatability was measured in the medium-sized nodes than in small nodes, and even higher repeatability in large nodular structures. In addition to this, Figure 8B shows that the mean susceptibilities decreased (became more diamagnetic) from small nodes to medium nodes, and again from medium nodes to larger nodular tissue. Moreover, the susceptibility histograms in these three ROI types (Figure 8C) were very similar on the diamagnetic (left) side, but showed different distributions on the paramagnetic (right) side. The histogram of the voxels in large nodular tissue (Figure 8C, black line) was relatively narrow and symmetric with a mean of around -0.2 ppm. While the mean susceptibilities were close to each other (within 0.1 ppm) for all three ROI types, there were more and more paramagnetic voxels in the medium (Figure 8C, blue line) and small

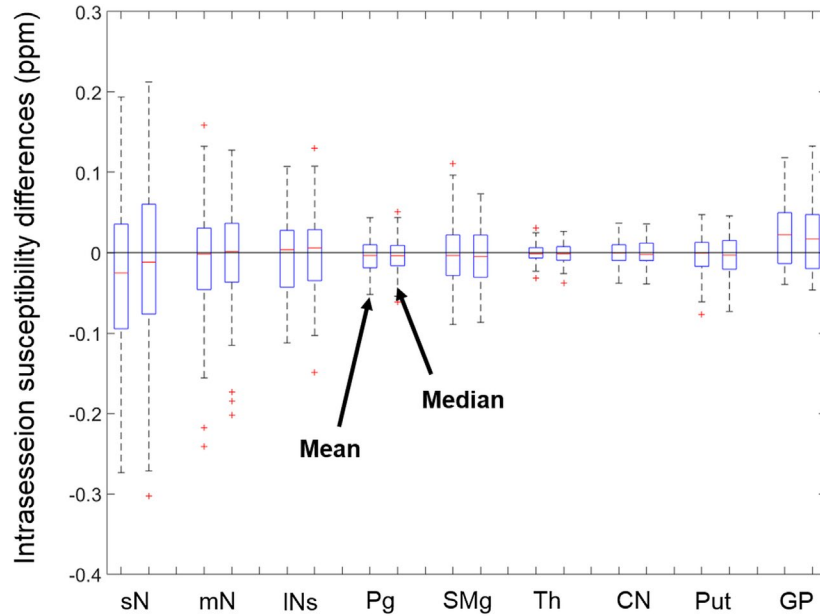


FIGURE 7 A comparison of the intrasession repeatability of the mean and median susceptibility. Box plots of intrasession mean and median susceptibility differences in different ROI types (red lines: medians, boxes: 25th and 75th percentiles, whiskers: most extreme data points not considered outliers, red crosses outliers): sN, small nodes ($VOL < 300 \text{ mm}^3$), mN, medium nodes ($VOL > 300 \text{ mm}^3$), INs, large nodular structures; Pg, parotid glands; SMg, submandibular glands; Th, thalamus; CN, caudate nucleus; Put, putamen; GP, globus pallidus. PDF and direct k-space inversion with Tikhonov regularisation were used for background field removal and susceptibility calculation, respectively, in each case

(Figure 8C, red line) nodes as the distributions became more positively skewed.

3.5 | Detectable effect sizes for different structures

Figure 9 compares distributions of the intrasession (top) and intersession (bottom) mean susceptibility differences. Standard deviations (SD) of susceptibility differences in each ROI type are also displayed at the bottom of each plot. Moreover, here the VOL- and SAD-based classifications of the small and medium lymph nodes are also compared. Note that all previous results were presented using the VOL-based classification, but the conclusions would be similar using the SAD-based classification (Supporting Information Figure S8). The repeatability was only marginally better for the VOL-based classification in most cases. The distributions of the intersession differences were generally broader than those of the intrasession differences and their means slightly further from zero in most cases. Both of these indicate higher intrasession than intersession repeatability in the HN.

Small nodes (either $VOL < 300 \text{ mm}^3$ or $SAD < 5 \text{ mm}$) had the worst repeatability (both intrasession and intersession) among all the tissue types followed by medium-sized nodes. Larger nodular structures (INs), the submandibular glands (SMg), and the globus pallidus (GP) had similar intrasession SDs (though the distribution of the GP had a median value greater than zero). The intersession repeatability of both the

INs and the SMg were closer to that of the medium-sized nodes. The GP had similar intrasession and intersession susceptibility difference distributions. Susceptibility measurements in the parotid glands, thalamus, caudate nucleus, and putamen were the most repeatable (both intrasession and intersession) out of all ROI types included in this study.

Minimum detectable effect sizes (MDEs) were calculated for all ROI types (Table 1) based on their intrasession and intersession susceptibility difference distributions. Small nodes had the highest MDEs ($\sim 0.3 \text{ ppm}$, that is, the worst repeatability) followed by medium-sized nodes ($\sim 0.2 \text{ ppm}$) and large nodular structures. Both large INs and SMg had low intrasession ($\sim 0.1 \text{ ppm}$) but much higher intersession MDEs ($\sim 0.2 \text{ ppm}$). Susceptibilities of brain regions were more repeatable than susceptibilities of most of the ROIs in the neck except the parotid gland which had very low MDEs both intrasession (0.06 ppm) and intersession (0.07 ppm). The calculated MDEs also indicate that intrasession repeatabilities are generally better than intersession repeatabilities as expected.

4 | DISCUSSION

Here we investigated the repeatability of an MRI acquisition protocol and QSM pipeline we optimized for measuring susceptibility in the HN region. We assessed both intrasession and intersession QSM repeatability in deep gray matter regions, the parotid and SMg, as well as in healthy lymph nodes using images acquired in 10 healthy volunteers. We

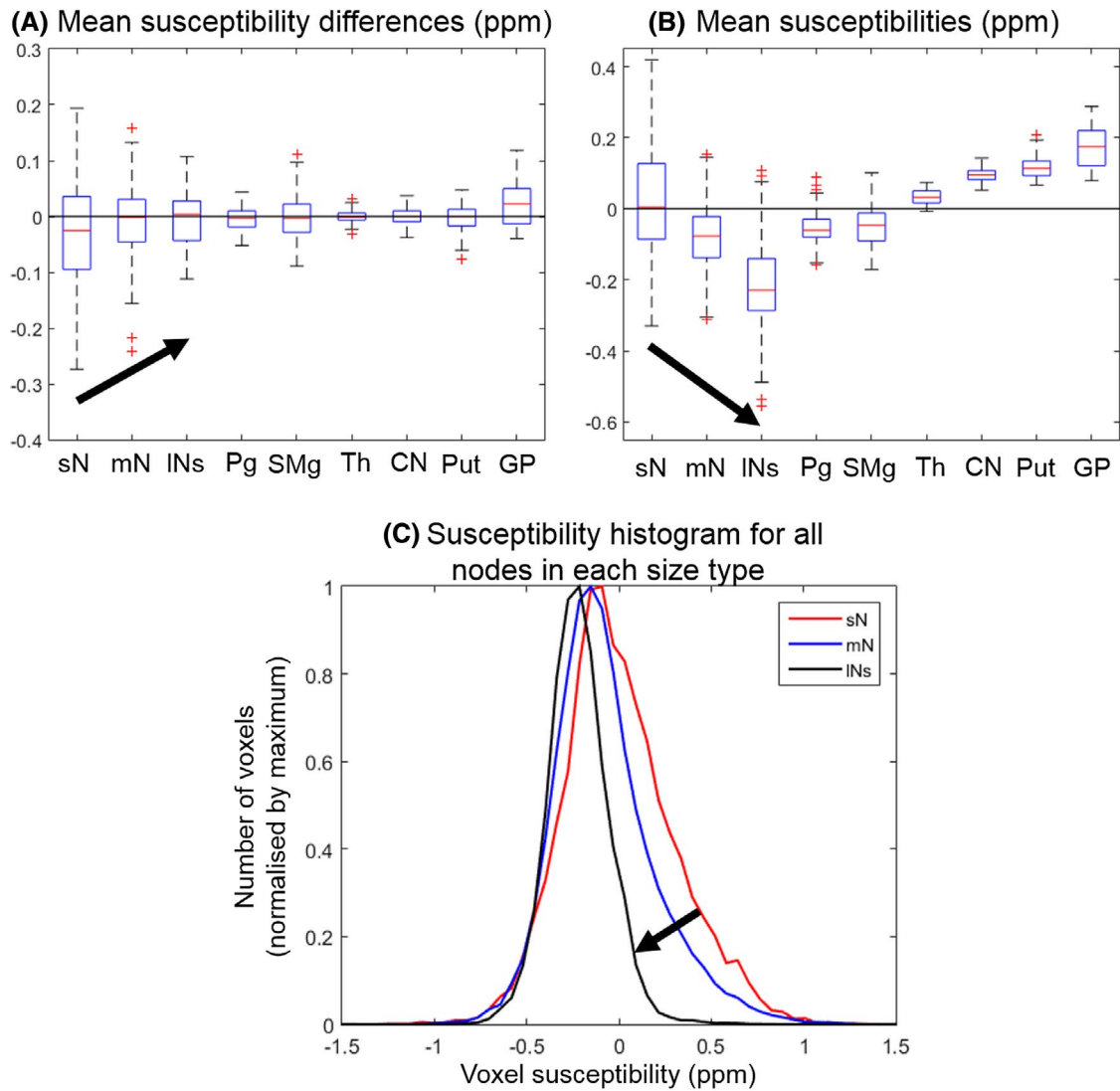


FIGURE 8 Susceptibility distributions and repeatability in lymph nodes of different sizes. Box plots of intrasession mean susceptibility differences (A) and mean susceptibilities (B) in different ROI types (red lines: medians, boxes: 25th and 75th percentiles, whiskers: most extreme data points not considered outliers, red crosses: outliers): sN, small nodes ($VOL < 300 \text{ mm}^3$), mN, medium nodes ($VOL > 300 \text{ mm}^3$), INs, large nodular structures; Pg, parotid glands; SMg, submandibular glands; Th, thalamus; CN, caudate nucleus; Put, putamen; GP, globus pallidus. Normalized susceptibility histograms of all voxels in sN, mN, or INs are also shown (C). PDF and direct k-space inversion with Tikhonov regularisation were used for background field removal and susceptibility calculation, respectively, in all cases

also compared the repeatability of the mean and median susceptibility as summary metrics within each region of interest (ROI). Projection onto Dipole Fields (PDF) provided more repeatable susceptibility maps in the HN region than the LBV background field removal (BFR) method (eg, Figure 6 top). There was no substantial difference between the repeatability of the two, Tikhonov regularisation-based susceptibility calculation methods we implemented here as these both performed equally well in the HN region (eg, Figure 6 bottom). In healthy volunteers, the mean and median susceptibilities within the ROIs seemed equally good metrics (eg, Figure 7) as most ROIs had a nearly symmetric susceptibility distribution (eg, Figure 3A). We calculated the MDEs for all ROI types. Intrasession repeatability was generally higher than

intersession repeatability as expected (eg, Figure 9) and QSM repeatability was higher in brain ROIs than in the neck.

Susceptibility maps were more repeatable using PDF, as opposed to LBV, combined with either of the two Tikhonov-regularisation-based susceptibility calculation techniques (eg, Figure 6 top). LBV assumes that the internal field contributions are constant zero at the tissue boundary.²² This might be a good approximation when the edges of the tissue mask are near regions with low susceptibility variations (eg, the susceptibility variations near the brain edges are below 0.1 ppm). In this case, field variations on the boundary induced by internal voxels near the boundary are negligible. However, for HN images, the susceptibility difference near the mask boundary is equal

FIGURE 9 The intrasession and intersession repeatability of the mean susceptibility. Box plots of intrasession (top) and intersession (bottom) mean susceptibility differences in different ROI types (red lines: medians, boxes: 25th and 75th percentiles, whiskers: most extreme data points not considered outliers, red crosses: outliers): sN, small nodes (both VOL < 300 mm³ and SAD < 5 mm are shown), mN, medium nodes (both VOL > 300 mm³ and SAD > 5 mm are shown), INs, large nodular structures; Pg, parotid glands; SMg, submandibular glands; Th, thalamus; CN, caudate nucleus; Put, putamen; GP, globus pallidus. PDF and direct k-space inversion with Tikhonov regularisation were used for background field removal and susceptibility calculation, respectively, in each case. Standard deviations (SD) of each distribution are displayed at the bottom of both plots

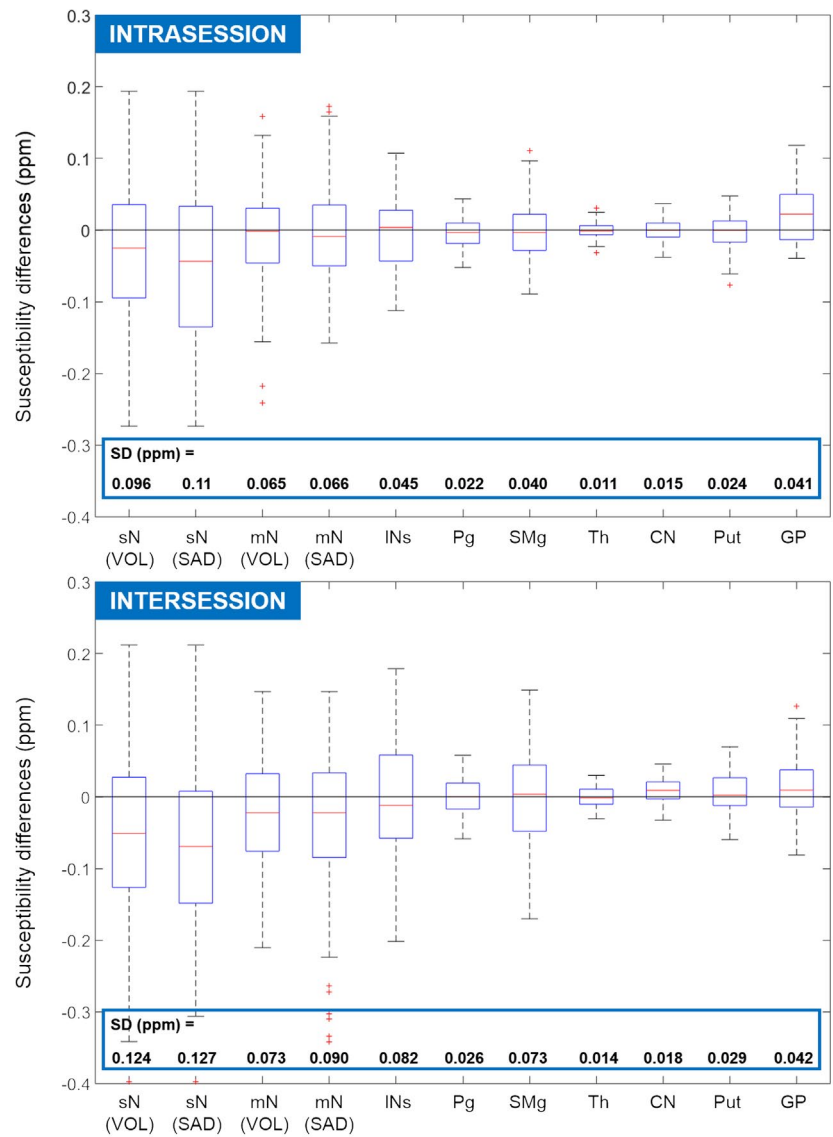


TABLE 1 Minimum detectable effect sizes (MDEs) as a measure of intrasession and intersession repeatability of the mean susceptibility

| Region of interest | Intrasession MDE (ppm) | Intersession MDE (ppm) |
|------------------------|------------------------|------------------------|
| Small lymph nodes | 0.27 | 0.32 |
| Medium lymph nodes | 0.16 | 0.22 |
| Large nodal structures | 0.11 | 0.20 |
| Parotid gland | 0.06 | 0.07 |
| Submandibular gland | 0.10 | 0.18 |
| Thalamus | 0.03 | 0.04 |
| Caudate nucleus | 0.04 | 0.05 |
| Putamen | 0.06 | 0.07 |
| Globus Pallidus | 0.10 | 0.10 |

Minimum detectable effect sizes (MDEs) calculated for each ROI type from the intrasession and intersession standard deviations of mean susceptibility differences. All susceptibility maps were calculated using PDF and direct k-space inversion with Tikhonov regularisation. Note that small and medium lymph nodes were classified based on their SAD as this metric is more commonly used in clinical practice.

to that of the tissue/air interface which is approximately 9.4 ppm.⁵⁶ In this case, internal voxels near the boundary have a significant contribution to the fields at the boundary and LBV's assumption is violated. Therefore, even though LBV has been shown to be one of the best BFR methods in the brain,²² it should be used with caution in anatomical regions containing air-tissue interfaces.

Iterative fitting in image space with Tikhonov regularisation seemed to provide susceptibility maps of slightly better repeatability in most ROIs in the neck (most lymph nodes, and the parotid and submandibular glands) compared to using direct k-space inversion. This is expected, as the iterative version accounts for the noise distribution within the tissue (by including the weighting term W) as opposed to the direct version (where W from Equation 1 is set to 1 across the entire volume). Moreover, the direct k-space inversion approach implicitly assumes that the measured field is zero outside of the tissue mask, while the iterative fitting approach does not. This could lead to errors in the measured susceptibility values for example, if the field perturbations induced

by an ROI extend beyond the tissue mask. However, both the repeatability, and the measured mean and median susceptibility values (Supporting Information Figures S9) were very similar for the two techniques which suggests that either the size or the susceptibility of the ROIs is too small for them to induce very large field perturbations. In brain regions and the large nodular structures, direct k-space inversion had slightly better repeatability than the iterative technique. Also, direct inversion is much faster (a few seconds) than the iterative approach (a few minutes). In summary, both susceptibility calculation techniques have similar repeatability in the HN of healthy volunteers and both techniques have potential advantages on a theoretical or computational level. It is interesting to note that these Tikhonov-regularisation-based methods outperformed other, more widely used methods in the HN region. Their MATLAB implementations will be made available on UCL's XIP repository: https://xip.uclb.com/i/software/TKD_dirTik_iterTik.html. Future work will involve comparing these Tikhonov-regularisation-based methods for HN QSM with other, emerging susceptibility calculation techniques from the 2019 QSM Reconstruction Challenge upon their release.

It is also important to note that while LPU is often criticized for reducing contrast in susceptibility maps, we have found that it is an extremely robust method in regions with complicated and highly wrapped phase where region-growing methods are more likely to fail. Also, though there is no standard way to create reliable tissue masks outside of the brain, our simple method of thresholding the inverse noise map at its mean was robust across 60 HN images (6 images for each of the 10 volunteers) even though the HN region is extremely heterogenous. Whether this automatic, 3D masking approach is applicable in other anatomical regions remains to be explored.

Our repeatability analysis does not show any substantial difference between using the mean or the median of the voxel susceptibilities within an ROI as a summary metric. This might be because the distribution of susceptibilities in most ROIs is roughly symmetric (eg, Figure 3A), therefore the mean and median are very similar. This might be the case for healthy subjects, but susceptibility distributions are likely to be much more skewed in diseased tissue.⁵⁷ Moreover, the median is a more robust summary metric for QSM in general.⁵⁸

Nodes classified based on their volume (VOL) or short-axis diameter (SAD) had similar repeatabilities, but the latter measure is more widely used in clinical practice. We have shown that the susceptibility distribution of smaller nodes was positively skewed. The histogram of large nodular structures was symmetric, whereas that of the medium nodes and especially the small nodes indicated more and more paramagnetic voxels included in the ROIs, most likely from the surrounding fatty voxels (Figure 4). In the HN region, most healthy

lymph nodes are located within the strongly paramagnetic fatty fascia between muscle sheets. If the ROIs are not drawn perfectly, some of these high-susceptibility voxels might be included by accident especially as the ROIs are propagated by imperfect image co-registration. Small lymph nodes were affected the most by this as they have relatively large surface areas compared to their volumes. Therefore small nodes had poor repeatability as their mean (and median) susceptibility was strongly affected by the number of accidentally included fatty voxels and this probably varied from scan to scan.

It could be argued that these trends in the repeatability of the susceptibility of nodes of different sizes are primarily introduced by the different number of voxels in the three ROI types, that is, averaging over more voxels gives a more reliable estimate and, therefore, corresponds to better repeatability. However, the large nodular structures segmented for this study had similar volumes (margins not included) to the small lymph nodes while the medium-sized nodes were generally larger. This indicates that the margin of a few millimeters on each side of the ROIs drawn inside the large nodular structures mitigated the effects of inaccurate segmentation leading to much better repeatability. Moreover, delineating the small lymph nodes across scans consistently was also challenging, because in some cases it was hard to identify the same small node in different scans. Incorrectly identified nodes might be another factor contributing to the relatively low repeatability of the small nodes. These observations also provide a guideline for future studies when lymph nodes are to be segmented in the HN region. To sum up, larger lymph nodes had better repeatability in general, but making sure that all surrounding fatty voxels are excluded from the ROI is even more important as these can confound the measured mean or median susceptibilities. Note that nodes reassigned based on their VOL or SAD had similar repeatabilities, but the latter measure is more widely used in clinical practice. Also note that while the pipeline in Figure 2 for segmentation of the lymph nodes was sufficient to perform this repeatability analysis, a robust, automated segmentation algorithm would be useful for future multi-centre HN studies.

Note that the susceptibilities of brain regions in Figure 8B are in accordance with previously measured values published in the QSM literature.^{6,11,47,59,60} This underscores the reliability of the susceptibility values and repeatability measured in other head-and-neck tissues (ie, glands and nodes). Also, all distributions of susceptibility differences in the brain were centred around zero apart from those of the small lymph nodes and the GP. We above explained how partial volume effects from the surrounding fatty fascia can confound susceptibility measurements in small nodes. A similar effect is expected in the GP as this structure is much more paramagnetic than its surroundings, so imperfect segmentation induces greater error. Susceptibility

values measured in the subcutaneous fat and muscle of the neck were in accordance with previously reported values (fat = 0.19-0.57 ppm, muscle = -0.36 and -0.16 ppm) in liver (ie, in the longissimus thoracis muscle^{7,18}) and knee⁵⁵ QSM. The susceptibility of the masseter muscle had especially low inter-subject variation which is encouraging because this muscle is located close to both the parotid and submandibular glands. The inter-subject variations in the subcutaneous fat and the semispinalis capitis muscle were higher due to some subject-dependent residual background fields at the back of the neck and because many of our subjects had very thin subcutaneous fat making it difficult to delineate this ROI accurately.

The intrasession repeatability was always better than or equal to the intersession repeatability for each region. This could be due to real biological changes and/or more errors in the ROI segmentations introduced by the intersession non-rigid image registration than the intrasession registration. The MDE needs to be calculated based on either the intrasession or the intersession standard deviations (SD) with the specific application in mind. Note that though QSM repeatability in the brain has been repeatedly investigated,²⁷⁻³² all previous studies used acquisition protocols and QSM pipelines optimized for the brain. Our protocol and pipeline, optimized specifically for the whole head-and-neck region, have several differences compared to state-of-the-art brain QSM acquisition and processing pipelines, including a slightly lower resolution to achieve sufficient signal-to-noise ratio in the neck and more motion artifacts introduced by the longer scan time. Most importantly, a HN mask was used for BFR and susceptibility calculation instead of a brain mask. Although achieving a clinically applicable scan time could potentially limit QSM accuracy and precision, the MRI protocol and QSM pipeline presented here are the result of careful and thorough optimisation and can be used as a benchmark for future, clinical QSM in the HN region. Nevertheless, our results show that the susceptibility of brain regions is repeatable even using the QSM pipeline optimized for the HN region. This could be important for applications targeting both the neck and the brain, for example investigating brain metastases of HPV-related head-and-neck cancer.⁶¹ Moreover, this study enables us to assess the repeatability of the selected HN regions by comparing these with the repeatabilities of the brain regions. For example, our results show that the parotid glands have very high QSM repeatability, comparable to that of the caudate nucleus. Considering that the susceptibility of the masseter muscle located near the parotid glands was in agreement with literature values across all subjects, and that the parotid lymph nodes were only visible in the susceptibility maps but not the magnitude images, we can conclude that our optimized acquisition protocol and QSM pipeline is especially accurate in and around the parotid glands.

Future applications of our optimized acquisition protocol and QSM pipeline for the HN region could include measuring tumour oxygenation⁶²⁻⁶⁴ in individual patients. Even if the susceptibility difference induced by smaller oxygenation-changes is likely to be confounded by the repeatability in individual patients, the distributions we measured here could be used for sample size calculations in, for example, clinical studies evaluating different oxygen-enhancement techniques to improve therapy⁶⁵ in HN cancer across the patient population. Another potential application is detecting the highly diamagnetic calcifications that tend to appear in thyroid nodules.⁶⁶⁻⁶⁸

5 | CONCLUSIONS

Here we introduced an optimized MRI acquisition protocol and susceptibility mapping pipeline tailored for QSM of the head-and-neck region and investigated its intrasession and intersession repeatability in deep gray matter regions, the parotid and submandibular glands and various healthy lymph nodes of different sizes.

We recommend the use of PDF for BFR in head-and-neck QSM as it provided more repeatable results than LBV. The two, Tikhonov-regularisation-based, susceptibility calculation methods we introduced here outperformed current, more widely used techniques in the head-and-neck region. These techniques had very similar repeatability and should be further compared in patient studies. While there was no substantial difference in using the mean or median as summary metrics within ROIs in this study, we suggest that the median should be used in patient studies as it is more robust in the skewed distributions expected in cancerous tissue. We also showed that careful delineation of ROIs is crucial to avoid inaccuracies, especially if the susceptibility difference between the region of interest and its surroundings is high, for example, for healthy lymph nodes embedded in paramagnetic fatty fascia.

We conclude that our optimized MRI protocol and QSM pipeline produced highly repeatable susceptibility maps in the brain, even though it is not optimized for brain imaging, and in the neck, especially in and around the parotid glands.

ACKNOWLEDGMENTS

We thank Magdalena Sokolska, Vincent Evans, and Leбина Kakkar for their help with the MRI acquisitions. Anita Karsa, EPSRC-funded UCL Centre for Doctoral Training in Medical Imaging: EP/L016478/1; Department of Health's National Institute for Health Research funded Biomedical Research Centre at University College London Hospitals; currently supported by Karin Shmueli's ERC Consolidator Grant DiSCo MRI SFN 770939. Shonit Punwani, Biomedical Research Centre; Cancer Research UK KCL/UCL Cancer Imaging Centre.

ORCID

Anita Karsa  <http://orcid.org/0000-0002-8648-3853>

Karin Shmueli  <http://orcid.org/0000-0001-7520-2975>

TWITTER

Anita Karsa  @MRI_phys_KS

REFERENCES

- Shmueli K, de Zwart JA, van Gelderen P, Li TQ, Dodd SJ, Duyn JH. Magnetic susceptibility mapping of brain tissue in vivo using MRI phase data. *Magn Reson Med*. 2009;62:1510-1522.
- de Rochefort L, Brown R, Prince MR, Wang Y. Quantitative MR susceptibility mapping using piece-wise constant regularized inversion of the magnetic field. *Magn Reson Med*. 2008;60:1003-1009.
- Wang Y, Liu T. Quantitative susceptibility mapping (QSM): decoding MRI data for a tissue magnetic biomarker. *Magn Reson Med*. 2015;73:82-101.
- Liu C, Li W, Tong KA, Yeom KW, Kuzminski S. Susceptibility-weighted imaging and quantitative susceptibility mapping in the brain. *J Magn Reson Imaging*. 2015;42:23-41.
- Jain V, Abdulmalik O, Probert KJ, Wehrli FW. Investigating the magnetic susceptibility properties of fresh human blood for non-invasive oxygen saturation quantification. *Magn Reson Med*. 2012;68:863-867.
- Bilgic B, Pfefferbaum A, Rohlfing T, Sullivan EV, Adalsteinsson E. MRI estimates of brain iron concentration in normal aging using quantitative susceptibility mapping. *NeuroImage*. 2012;59:2625-2635.
- Sharma SD, Fischer R, Schoennagel BP, et al. MRI-based quantitative susceptibility mapping (QSM) and R2* mapping of liver iron overload: Comparison with SQUID-based biomagnetic liver susceptometry. *Magn Reson Med*. 2017;78:264-270.
- Straub S, Laun FB, Emmerich J, et al. Potential of quantitative susceptibility mapping for detection of prostatic calcifications. *J Magn Reson Imaging*. 2017;45:889-898.
- Biondetti E, Rojas-Villabona A, Sokolska M, et al. Investigating the oxygenation of brain arteriovenous malformations using quantitative susceptibility mapping. *NeuroImage*. 2019;199:440-453.
- Eskreis-Winkler S, Zhang Y, Zhang J, et al. The clinical utility of QSM: disease diagnosis, medical management, and surgical planning. *NMR Biomed*. 2017;30:e3668.
- Langkammer C, Schweser F, Krebs N, et al. Quantitative susceptibility mapping (QSM) as a means to measure brain iron? *A post mortem validation study*. *NeuroImage*. 2012;62:1593-1599.
- Wisnieff C, Ramanan S, Olesik J, Gauthier S, Wang Y, Pitt D. Quantitative susceptibility mapping (QSM) of white matter multiple sclerosis lesions: interpreting positive susceptibility and the presence of iron. *Magn Reson Med*. 2015;74:564-570.
- Li X, Harrison DM, Liu H, et al. Magnetic susceptibility contrast variations in multiple sclerosis lesions. *J Magn Reson Imaging*. 2016;43:463-473.
- Du G, Liu T, Lewis MM, et al. Quantitative susceptibility mapping of the midbrain in Parkinson's disease. *Movement Disorders*. 2016;31:317-324.
- He N, Ling H, Ding B, et al. Region-specific disturbed iron distribution in early idiopathic Parkinson's disease measured by quantitative susceptibility mapping. *Human Brain Mapping*. 2015;36:4407-4420.
- Barbosa JHO, Santos AC, Tumas V, et al. Quantifying brain iron deposition in patients with Parkinson's disease using quantitative susceptibility mapping, R2 and R2*. *Magn Reson Imaging*. 2015;33:559-565.
- Ng AC, Poudel G, Stout JC, et al. Iron accumulation in the basal ganglia in Huntington's disease: cross-sectional data from the IMAGE-HD study. *J Neurol. Neurosurgery Psychiatry*. 2015;87(5):545-549.
- Dong J, Liu T, Chen F, et al. Simultaneous phase unwrapping and removal of chemical shift (SPURS) using graph cuts: application in quantitative susceptibility mapping. *IEEE Trans Med Imaging*. 2015;34:531-540.
- Dimov AV, Liu T, Spincemaille P, et al. Joint estimation of chemical shift and quantitative susceptibility mapping (chemical QSM). *Magn Reson Med*. 2015;73:2100-2110.
- Karsa A, Punwani S, Shmueli K. Fat Correction of MRI Phase Images For Accurate Susceptibility Mapping in the Head-and-Neck. In: Proceedings of ISMRM 26th Annual Meeting, Paris; 2018:4988.
- Robinson SD, Bredies K, Khabipova D, Dymerska B, Marques JP, Schweser F. An illustrated comparison of processing methods for MR phase imaging and QSM: combining array coil signals and phase unwrapping. *NMR Biomed*. 2016;30:e3601
- Schweser F, Robinson SD, de Rochefort L, Li W, Bredies K. An illustrated comparison of processing methods for phase MRI and QSM: removal of background field contributions from sources outside the region of interest. *NMR Biomed*. 2017;30:e3604.
- Langkammer C, Schweser F, Shmueli K, et al. Quantitative susceptibility mapping: report from the 2016 reconstruction challenge. *Magn Reson Med*. 2018;79:1661-1673.
- Zhou D, Cho J, Zhang J, Spincemaille P, Wang Y. Susceptibility underestimation in a high-susceptibility phantom: dependence on imaging resolution, magnitude contrast, and other parameters. *Magn Reson Med*. 2017;78:1080-1086.
- Elkady AM, Sun H, Wilman AH. Importance of extended spatial coverage for quantitative susceptibility mapping of iron-rich deep gray matter. *Magn Reson Imaging*. 2016;34:574-578.
- Karsa A, Punwani S, Shmueli K. The effect of low resolution and coverage on the accuracy of susceptibility mapping. *Magn Reson Med*. 2019;81:1833-1848.
- Hinoda T, Fushimi Y, Okada T, et al. Quantitative susceptibility mapping at 3 T and 1.5 T: evaluation of consistency and reproducibility. *Investigative Radiol*. 2015;50:522-530.
- Ogasawara A, Kakeda S, Watanabe K, et al. Quantitative susceptibility mapping in patients with systemic lupus erythematosus: detection of abnormalities in normal-appearing basal ganglia. *Eur Radiol*. 2016;26:1056-1063.
- Deh K, Nguyen TD, Eskreis-Winkler S, et al. Reproducibility of quantitative susceptibility mapping in the brain at two field strengths from two vendors. *J Magn Reson Imaging*. 2015;42:1592-1600.
- Lin PY, Chao TC, Wu ML. Quantitative susceptibility mapping of human brain at 3T: a multisite reproducibility study. *Am J Neuroradiol*. 2015;36:467-474.
- Santin M, Didier M, Valabregue R, et al. Reproducibility of R2* and quantitative susceptibility mapping (QSM) reconstruction methods in the basal ganglia of healthy subjects. *NMR Biomed*. 2017;30:e3491.
- Feng X, Deistung A, Reichenbach JR. Quantitative susceptibility mapping (QSM) and R2* in the human brain at 3 T: evaluation

- of intra-scanner repeatability. *Zeitschrift für Medizinische Physik*. 2018;28:36-48.
33. Karsa, A. 2018. *Optimising MRI Magnetic Susceptibility Mapping for Applications in Challenging Regions of the Body* [Thesis (PhD)]. London: University College. https://discovery.ucl.ac.uk/id/eprint/10064348/1/Anita_Karsa_PhDThesis.pdf
 34. Kressler B, de Rochefort L, Liu T, Spincemaille P, Jiang Q, Wang Y. Nonlinear regularization for per voxel estimation of magnetic susceptibility distributions from MRI field maps. *IEEE Trans Med Imaging*. 2010;29:273.
 35. Schweser F, Deistung A, Sommer K, Reichenbach JR. Toward on-line reconstruction of quantitative susceptibility maps: superfast dipole inversion. *Magn Reson Med*. 2013;69:1581-1593.
 36. Karsa A, Punwani S, Shmueli K. High repeatability of quantitative susceptibility mapping (QSM) in the head and neck with a view to detecting hypoxic cancer sites. In: Proceedings of ISMRM 27th Annual Meeting, Montreal; 2019:4939.
 37. Pruessmann KP, Weiger M, Scheidegger MB, Boesiger P, et al. SENSE: sensitivity encoding for fast MRI. *Magn Reson Med*. 1999;42:952-962.
 38. Liu T, Wisnieff C, Lou M, Chen W, Spincemaille P, Wang Y. Nonlinear formulation of the magnetic field to source relationship for robust quantitative susceptibility mapping. *Magn Reson Med*. 2013;69:467-476.
 39. Cornell MRL. *MEDI toolbox*: <http://weill.cornell.edu/mri/pages/qsm.html>
 40. Biondetti E, Thomas DL, Shmueli K. Application of Laplacian-based methods to multi-echo phase data for accurate susceptibility mapping. In: Proceedings of ISMRM 24th Annual Meeting, Singapore; 2016:1547.
 41. Karsa A, Shmueli K. SEGUE: a speedy rEGion-growing algorithm for unwrapping estimated phase. *IEEE Trans Med Imaging*. 2018;38:1347-1357.
 42. Liu T, Khalidov I, de Rochefort L, et al. A novel background field removal method for MRI using projection onto dipole fields (PDF). *NMR Biomed*. 2011;24:1129-1136.
 43. Zhou D, Liu T, Spincemaille P, Wang Y. Background field removal by solving the Laplacian boundary value problem. *NMR Biomed*. 2014;27:312-319.
 44. Liu J, Liu T, de Rochefort L, et al. Morphology enabled dipole inversion for quantitative susceptibility mapping using structural consistency between the magnitude image and the susceptibility map. *NeuroImage*. 2012;59:2560-2568.
 45. Hansen PC, O'Leary DP. The use of the L-curve in the regularization of discrete ill-posed problems. *SIAM J Sci Comput*. 1993;14:1487-1503.
 46. Li W, Wang N, Yu F, et al. A method for estimating and removing streaking artifacts in quantitative susceptibility mapping. *Neuroimage*. 2015;108:111-122.
 47. Sun H, Wilman AH. Background field removal using spherical mean value filtering and Tikhonov regularization. *Magn Reson Med*. 2014;71:1151-1157.
 48. Patenaude B, Smith SM, Kennedy DN, Jenkinson M. A Bayesian model of shape and appearance for subcortical brain segmentation. *Neuroimage*. 2011;56:907-922.
 49. Yushkevich PA, Piven J, Hazlett HC, et al. User-guided 3D active contour segmentation of anatomical structures: significantly improved efficiency and reliability. *NeuroImage*. 2006;31:1116-1128.
 50. ITK-SNAP software package: <http://www.itksnap.org/pmwiki/pmwiki.php>
 51. Rueckert D, Sonoda LI, Hayes C, Hill DL, Leach MO, Hawkes DJ. Nonrigid registration using free-form deformations: application to breast MR images. *IEEE Trans Med Imaging*. 1999;18:712-721.
 52. Lee S, Wolberg G, Shin SY. Scattered data interpolation with multilevel B-splines. *IEEE Trans Visualization Comput Graph*. 1997;3:228-244.
 53. MATLAB b-spline: <https://uk.mathworks.com/matlabcentral/fileexchange/20057-b-spline-grid-image-and-point-based-registration>
 54. Bloom HS. Minimum detectable effects: a simple way to report the statistical power of experimental designs. *Evaluation Rev*. 1995;19:547-556.
 55. Wei H, Dibb R, Decker K, et al. Investigating magnetic susceptibility of human knee joint at 7 Tesla. *Magn Reson Med*. 2017;78:1933-1943.
 56. Schenck JF. The role of magnetic susceptibility in magnetic resonance imaging: MRI magnetic compatibility of the first and second kinds. *Med Phys*. 1996;23:815-850.
 57. McPhail LD, Robinson SP. Intrinsic susceptibility MR imaging of chemically induced rat mammary tumors: relationship to histologic assessment of hypoxia and fibrosis. *Radiology*. 2009;254:110-118.
 58. Dixon E. 2018. *Applications of MRI magnetic susceptibility mapping in PET-MRI brain studies* [Thesis (PhD)]. University College London. <https://www.ucl.ac.uk/library/>
 59. Liu Z, Kee Y, Zhou D, Wang Y, Spincemaille P. Preconditioned total field inversion (TFI) method for quantitative susceptibility mapping. *Magn Reson Med*. 2017;78:303-315.
 60. Deistung A, Schäfer A, Schweser F, Biedermann U, Turner R, Reichenbach JR. Toward in vivo histology: a comparison of quantitative susceptibility mapping (QSM) with magnitude-, phase-, and R2*-imaging at ultra-high magnetic field strength. *NeuroImage*. 2013;65:299-314.
 61. Ruzevick J, Olivi A, Westra WH. Metastatic squamous cell carcinoma to the brain: an unrecognized pattern of distant spread in patients with HPV-related head and neck cancer. *J Neuro-Oncol*. 2013;112:449-454.
 62. Baudalet C, Gallez B. How does blood oxygen level-dependent (BOLD) contrast correlate with oxygen partial pressure (pO₂) inside tumors? *Magn Reson Med*. 2002;48:980-986.
 63. Panek R, Welsh L, Dunlop A, et al. Repeatability and sensitivity of measurements in patients with head and neck squamous cell carcinoma at 3T. *J Magn Reson Imaging*. 2016;44:72-80.
 64. Özbay PS, Stieb S, Rossi C, et al. Lesion magnetic susceptibility response to hyperoxic challenge: a biomarker for malignant brain tumor microenvironment? *Magn Reson Imaging*. 2018;47:147-153.
 65. Overgaard J. Hypoxic modification of radiotherapy in squamous cell carcinoma of the head and neck—a systematic review and meta-analysis. *Radiotherapy Oncol*. 2011;100:22-32.
 66. Kakkos SK, Scopa CD, Chalmoukis AK, et al. Relative risk of cancer in sonographically detected thyroid nodules with calcifications. *J Clin Ultrasound*. 2000;28:347-352.
 67. Seiberling KA, Dutra JC, Grant T, Bajramovic S. Role of intrathyroidal calcifications detected on ultrasound as a marker of malignancy. *The Laryngoscope*. 2004;114:1753-1757.

68. Lu Z, Mu Y, Zhu H, et al. Clinical value of using ultrasound to assess calcification patterns in thyroid nodules. *World J Surgery*. 2011;35:122-127.

SUPPORTING INFORMATION

Additional Supporting Information may be found online in the Supporting Information section.

FIGURE S1 Optimising the resolution and the SENSE factors.³³ Example coronal slices of the calculated susceptibility maps for the four different acquisition protocols (columns) used in the same volunteer are shown. The magnitude SNRs are displayed below the images

FIGURE S2 Sagittal slices of the last-echo magnitude images³³ and corresponding susceptibility maps of the two acquisitions with 1.25 mm isotropic resolution and different SENSE acceleration factors. The yellow ellipses highlight that a 2×1 acceleration (left) provides better visibility of lymph nodes in the AP direction

FIGURE S3 Comparison of two different techniques for removing residual phase wraps after nonlinear field fitting.³³ The arrows show a residual wrap in the region-growing (SEGUE) unwrapped field map toward the mask edges that is not present in the Laplacian phase unwrapping (LPU) result. The computation times are also shown

FIGURE S4 A comparison of the **intersession** repeatability of the mean susceptibility calculated using different background field removal techniques. Box plots of intrasession mean susceptibility differences in different ROI types (red lines-medians, boxes-25th and 75th percentiles, whiskers-most extreme data points not considered outliers, red crosses-outliers): sN, small nodes ($VOL < 300 \text{ mm}^3$); mN, medium nodes ($VOL > 300 \text{ mm}^3$); INs, large nodular structures; Pg, parotid glands; SMg, submandibular glands; Th, thalamus; CN, caudate nucleus; Put, putamen, GP, globus pallidus. For each ROI type, distributions on the left and right sides correspond to susceptibility maps obtained using PDF or LBV, respectively (see arrows). All measured susceptibilities were calculated using **direct k-space inversion** with Tikhonov regularisation

FIGURE S5 A comparison of the **intrasession** repeatability of the mean susceptibility calculated using different background field removal techniques. Box plots of intrasession mean susceptibility differences in different ROI types (red lines-medians, boxes-25th and 75th percentiles, whiskers-most extreme data points not considered outliers; red crosses-outliers): sN, small nodes ($VOL < 300 \text{ mm}^3$); mN, medium nodes ($VOL > 300 \text{ mm}^3$); INs, large nodular structures; Pg, parotid glands; SMg, submandibular glands; Th, thalamus; CN, caudate nucleus; Put, putamen, GP, globus pallidus. For each ROI type, distributions on the left and right

sides correspond to susceptibility maps obtained using PDF or LBV, respectively (see arrows). All measured susceptibilities were calculated using **iterative fitting** with Tikhonov regularisation

FIGURE S6 A comparison of the **intersession** repeatability of the mean susceptibility calculated using different background field removal techniques. Box plots of intrasession mean susceptibility differences in different ROI types (red lines-medians, boxes-25th and 75th percentiles, whiskers-most extreme data points not considered outliers, red crosses-outliers): sN, small nodes ($VOL < 300 \text{ mm}^3$); mN, medium nodes ($VOL > 300 \text{ mm}^3$); INs, large nodular structures; Pg, parotid glands; SMg, submandibular glands; Th, thalamus; CN, caudate nucleus; Put, putamen; GP, globus pallidus. For each ROI type, distributions on the left and right sides correspond to susceptibility maps obtained using PDF or LBV, respectively (see arrows). All measured susceptibilities were calculated using **iterative fitting** with Tikhonov regularisation

FIGURE S7 A comparison of the **intersession** repeatability of the mean susceptibility calculated using different Tikhonov-based regularisation techniques. Box plots of intrasession mean susceptibility differences in different ROI types (red lines-medians, boxes-25th and 75th percentiles, whiskers-most extreme data points not considered outliers, red crosses-outliers): sN, small nodes ($VOL < 300 \text{ mm}^3$); mN, medium nodes ($VOL > 300 \text{ mm}^3$); INs, large nodular structures; Pg, parotid glands; SMg, submandibular glands; Th, thalamus; CN, caudate nucleus; Put, putamen; GP, globus pallidus. For each ROI type, distributions on the left and right sides correspond to susceptibility maps calculated using direct k-space inversion or iterative fitting, respectively (see arrows). PDF was used for background field removal in each case

FIGURE S8 A comparison of the intrasession repeatability of the mean susceptibility using VOL- or SAD-based classification of lymph nodes. Box plots of intrasession mean susceptibility differences in different ROI types (red lines-medians, boxes-25th and 75th percentiles, whiskers-most extreme data points not considered outliers, red crosses-outliers). Left image: A comparison of the PDF and LBV background field removal methods. For each ROI type, distributions on the left and right sides correspond to susceptibility maps calculated using PDF or LBV, respectively (see arrows). Direct k-space inversion was used for susceptibility calculation in each case. Right image: A comparison of the direct and iterative Tikhonov methods. For each ROI type, distributions on the left and right sides correspond to susceptibility maps calculated using direct k-space inversion or iterative fitting, respectively (see arrows). PDF was used for background field removal in each case

FIGURE S9 Bland-Altman plot of mean susceptibilities measured in every segmented ROI calculated using either direct k-space inversion or iterative fitting. The blue line indicates the mean of the differences, while the red dashed lines correspond to the 2.5th and 97.5th percentiles. The black ellipse highlights that the mean susceptibilities calculated in the diamagnetic lymph nodes are especially similar for these two susceptibility calculation techniques

How to cite this article: Karsa A, Punwani S, Shmueli K, et al. MAn optimized and highly repeatable MRI acquisition and processing pipeline for quantitative susceptibility mapping in the head-and-neck region. *Magn Reson Med*. 2020;00:1–17. <https://doi.org/10.1002/mrm.28377>